REPORT DOCUMENTATION PAGE

1. REPORT DATE *(DD-MM-YYYY)*	2. REPORT TYPE	3. DATES COVERED *(From - To)*
06/29/2012	Final Technical Report	March 2010 - February 2012

4. TITLE AND SUBTITLE

RECONFIGURABLE OPTICAL ELEMENTS BASED ON SINGLE AND COUPLED MICRODISK RESONATORS WITH QUANTUM DOT ACTIVE MEDIA

5a. CONTRACT NUMBER
FA9550-10-C-0055

5b. GRANT NUMBER

5c. PROGRAM ELEMENT NUMBER

6. AUTHOR(S)
Dr. Vinod Menon

5d. PROJECT NUMBER

5e. TASK NUMBER

5f. WORK UNIT NUMBER

7. PERFORMING ORGANIZATION NAME(S) AND ADDRESS(ES)
HYBRID PHOTONICS, LLC
104 ADDISON LN
GREENVALE NY 11548-1130

8. PERFORMING ORGANIZATION REPORT NUMBER
HYB0008Z

9. SPONSORING/MONITORING AGENCY NAME(S) AND ADDRESS(ES)
AF OFFICE OF SCIENTIFIC RESEARCH
875 N. RANDOLPH ST. ROOM 3112
ARLINGTON VA 22203

10. SPONSOR/MONITOR'S ACRONYM(S)
AFSOR

11. SPONSOR/MONITOR'S REPORT NUMBER(S)
AFRL-OSR-VA-TR-2012-0938

12. DISTRIBUTION/AVAILABILITY STATEMENT

Distribution A: Approved for Public Release

13. SUPPLEMENTARY NOTES

14. ABSTRACT

We developed a low cost technique for incorporating colloidal quantum dots into active photonic structures with the end goal of realizing bistable lasing structures. To this end we successfully demonstrated (i) incorporation of CdSe QDs into polymer and dielectric host and realization of devices such as active waveguides, microdisk and microring resonators, surface emitting microcavity structures, and distributed feedback (DFB) grating structures, (ii) gain and amplified spontaneous emission (ASE) from a vertical cavity surface emitting structure, (iii) gain and lasing like emission from planar DFB grating structures fabricated using softlithography, (iv) protocol for developing surface emitting and DFB lasers using colloidal QDs as the active medium and (v) theoretical models for coupled/single resonator bistable

15. SUBJECT TERMS

STTR Report, Reconfigurable Optical Elements, Hysteresis, Microdisk Resonators, Quantum Dots, Lasers, Bistability

16. SECURITY CLASSIFICATION OF:			17. LIMITATION OF ABSTRACT	18. NUMBER OF PAGES	19a. NAME OF RESPONSIBLE PERSON
a. REPORT	b. ABSTRACT	c. THIS PAGE			Vinod Menon
U	U	U	UU	29	19b. TELEPHONE NUMBER *(Include area code)* (609) 575-1752

Final Report

Period: March 1ˢᵗ, 2010 – June 30ᵗʰ 2012
Project: Reconfigurable Optical Elements Based on Single and Coupled Microdisk Resonators with Quantum Dot Active Media

Principal Investigator: Dr. Vinod Menon
Hybrid Photonics, LLC
104 Addison Lane, Greenvale, NY 11548
Phone: 347-746-8661, E-mail: menon@hybridphotonics.com

1. Introduction

The main objective of our STTR Phase II program is to design and build a chip-scale cost effective reconfigurable optical device that relies on lasing bistability in a system of single and coupled microresonators with embedded quantum dots (QDs).

Relevance: Military decision making at both tactical and strategic levels crucially depends on capabilities for real time processing of large amounts of information. All-optical platforms are viewed as the main technology capable of delivering the required speed for information processing. The reconfigurable photonic device being developed by Hybrid Photonics will play the role of a transistor in photonic integrated circuits providing all-optical signal processing at speeds exceeding Tbits/second and low power consumption.

Approach: Two different systems were pursued for realizing reconfigurable optical systems that show all-optical bistability. The first system consists of coupled microresonators. Here microdisks, microring, vertical cavity structures and coupled distributed feedback structures were investigated to obtain bistable lasing modes. The second system consisted of a passive microring resonator coupled to two bus waveguides which have an integrated gain medium. The active material in all of these systems is colloidal quantum dots. While the present demonstrations were carried out using CdSe/ZnS dots that emit in the red, we can easily extend the present work into the infrared using PbSe QDs.

Summary: The biggest challenge in the phase II program was the incorporation of colloidal QDs into host materials that do not affect their optical properties while being able to be patterned into photonic structures. The following are the significant outcomes of the program:

- Successful incorporation of CdSe QDs into polymer and dielectric host and realization of devices such as active waveguides, microdisk and microring resonators, surface emitting microcavity structures, and distributed feedback (DFB) grating structures

- Demonstration of gain and amplified spontaneous emission (ASE) from a vertical cavity surface emitting structure.

- Demonstration of gain and lasing like emission from planar DFB grating structures fabricated using softlithography.

- Development of fabrication protocol for developing surface emitting and DFB lasers using colloidal QDs as the active medium.

- Development of theoretical models for coupled/single resonator bistable lasing structures.

2. Coupled Microresonator System

2.1 Theory and Software Development

Theory/software component under this approach involved the development of simulation tools for modeling the lasing characteristics of coupled microdisks/ring resonators. We also performed finite difference time domain simulations to model the electromagnetic field distributions in the coupled resonator system.

2.1.1 Modes of passive disks

In the course of the project we developed a model and corresponding software for computing modes of the coupled disks structures using generalization of the "constant-flux-mode" approach [1,2], which was applied to a single disk problem during Phase I of the project. We consider i-th disk of radius R_i and refractive index n_d whose center is positioned at $\mathbf{r} = \mathbf{r}_i$ and introduce internal field inside the i-th disk as a linear combination of Bessel functions of the first kind, $J_m(x)$

$$F_{\text{int}}^{(i)} = \sum_m d_m^{(i)} e^{im\varphi} J_m\left(n_d k_{ms} |\mathbf{r} - \mathbf{r}_i|\right) \tag{1}$$

where k_{ms} is the eigenfrequency of the coupled system (we use the system of units, in which speed of light in vacuum is unity) characterized by the azimuthal number m and radial number s. The field scattered by the i-th disk is introduced via linear combination of Hankel functions of the first kind, $H_m(x)$

$$F_{sc} = \sum_m b_m^{(i)} e^{im\varphi_i} H_m\left(n_0 k |\mathbf{r} - \mathbf{r}_i|\right) \tag{2}$$

where n_0 is the refractive index of the external medium, and k is a free spectral parameter representing frequency of out outgoing stationary lasing output. The distinction between outside spectral parameter and the eigenvalues of the system (which become functions of k) is the characteristic feature of the constant-flux-mode approach [1,2]. Function F in Eq. (2) represents normal to the disk component of the magnetic field for TE polarization and that of electric field for TM polarization. The field incident on this disk consists of the fields scattered by all other disks:

$$F_{inc}^{(i)} = \sum_{j \neq i} \sum_m b_m^{(j)} e^{im\varphi_j} H_m\left(n_0 k |\mathbf{r} - \mathbf{r}_j|\right) \tag{3}$$

where polar angles φ_j and radial coordinates are defined in local coordinate systems associated with each $j - th$ disk. In order to be able to use boundary conditions at the rim of the $i - th$ disk we need to rewrite the scattered field in the coordinate system centered at the $i - th$ disk. This is achieved with the help of Graffs formula for the Hankel function [3]

$$e^{im\varphi_j} H_m\left(n_0 k \left|\mathbf{r}-\mathbf{r}_j\right|\right) = \sum_{n=-\infty}^{n=\infty} H_{n-m}\left(n_0 k R_{ji}\right) e^{i(m-n)\theta_{ji}} J_n\left(n_0 k \left|\mathbf{r}-\mathbf{r}_i\right|\right) e^{in\varphi_i} \tag{4}$$

where R_{ji} and θ_{ji} are radial and polar coordinates of the $i-th$ disk in the coordinate system centered at $j-th$ disk. Using standard Maxwell boundary conditions at the rim of the disk we derive for the expansion coefficients of the internal field

$$d_m^{(i)} = \tilde{\alpha}_m^{(i)}(k,k_{m,s}) \sum_{j \neq i} \sum_n \kappa_n^{(j)} d_n^{(j)} H_{m-n}\left(n_0 k R_{ji}\right) e^{i(n-m)\theta_{ji}} \tag{5}$$

where

$$\tilde{\alpha}_m^{(i)}(k,k_{m,s}) = \begin{cases} -\dfrac{2in_{d,i}}{\pi n_0 R_i} \dfrac{1}{n_0 k_{ms} H_m\left(kn_0 R_i\right) J_m'\left(k_{ms} n_d R_i\right) - kn_d J_m\left(k_{ms} n_d R_i\right) H_m'\left(kn_0 R_i\right)}, TE \\[4mm] -\dfrac{2i}{\pi R_i} \dfrac{1}{n_d k_{ms} H_m\left(kn_0 R_i\right) J_m'\left(k_{ms} n_d R_i\right) - kn_o J_m\left(k_{ms} n_d R_i\right) H_m'\left(kn_0 R_i\right)}, TM \end{cases} \tag{6}$$

and

$$\kappa_m^{(i)}(k_{ms},k) = \begin{cases} i\dfrac{\pi R_i}{2}\left[kn_0 J_m'\left(kn_0 R_i\right) J_m\left(n_d k_{ms} R_i\right) - n_d k_{ms} J_m'\left(n_d k_{ms} R_i\right) J_m\left(kn_0 R_i\right)\right] \\[4mm] i\dfrac{\pi n_0 R_i}{2n_d}\left[kn_d J_m'\left(kn_0 R_i\right) J_m\left(n_d k_{ms} R_i\right) - n_0 k_{ms} J_m'\left(n_d k_{ms} R_i\right) J_m\left(kn_0 R_i\right)\right] \end{cases} \tag{7}$$

In the case of only two disks we can choose the axis of the coordinate system along their centers so that $\theta_{12} = 0; \theta_{21} = \pi$ and Eq. (5) takes the following form

$$\begin{aligned} d_m^{(1)} &= \tilde{\alpha}_m^{(1)}(k,k_s) \sum_n \kappa_n^{(2)} d_n^{(2)} H_{m-n}\left(n_0 k R_{12}\right) \\ d_m^{(2)} &= \tilde{\alpha}_m^{(2)}(k,k_s) \sum_n \kappa_n^{(1)} d_n^{(1)} H_{m-n}\left(n_0 k R_{12}\right) \end{aligned} \tag{8}$$

For high-Q resonances, the largest contribution to the sum over modes in Eq. (8) comes from the term with $n = -m$. In this resonant approximation we have

$$\begin{aligned} d_m^{(1)} &= \tilde{\alpha}_m^{(1)}(k,k_s)\kappa_m^{(2)} t_{2m} d_{-m}^{(2)}; \quad d_{-m}^{(2)} = \tilde{\alpha}_m^{(2)}(k,k_s)\kappa_m^{(1)} t_{2m} d_m^{(1)} \\ d_{-m}^{(1)} &= \tilde{\alpha}_m^{(1)}(k,k_s)\kappa_m^{(2)} t_{2m} d_m^{(2)}; \quad d_m^{(2)} = \tilde{\alpha}_m^{(2)}(k,k_s)\kappa_m^{(1)} t_{2m} d_{-m}^{(1)} \end{aligned} \tag{9}$$

where we introduced a coupling constant

$$t_{2m} = H_{2m}\left(n_0 k R_{12}\right) \tag{10}$$

The system of equations (9) describes two pairs of degenerate modes, whose eigenfrequencies are given by equation:

$$1 = \tilde{\alpha}_m^{(1)}(k, k_s)\tilde{\alpha}_m^{(2)}(k, k_s)\kappa_m^{(1)}\kappa_m^{(2)}\left(t_{2m}\right)^2 \tag{11}$$

This equation has two solutions in the vicinity of $m-th$ mode, which we will designate as $k_{m,1}$ and $k_{m,2}$. In order to look for these solutions numerically we exploit the same algorithm that we used for a single disk problem in the Phase I. In order to find the starting points we can try to use the following approach. If the disks are identical (or almost identical), we present the scattering coefficients in the vicinity of the single disk solutions as

$$\tilde{\alpha}_m^{(1)}(k, k_s)\kappa_m^{(1)} = \frac{-i\gamma_{m,s}^{(1)}}{k - k_s + i\gamma_{m,s}^{(1)}}$$

$$\tilde{\alpha}_m^{(2)}(k, k_s)\kappa_m^{(2)} = \frac{-i\gamma_{m,s}^{(2)}}{k - k_s + i\gamma_{m,s}^{(2)}} \tag{12}$$

Eq. (11) then takes the form of

$$\frac{-i\gamma_{m,s}^{(1)}}{k - k_s + i\gamma_{m,s}^{(1)}}\frac{-i\gamma_{m,s}^{(2)}}{k - k_s + i\gamma_{m,s}^{(2)}}\left(t_{2m}\right)^2 = 1$$

$$\left[k - k_s + i\gamma_{m,s}^{(1)}\right]\left[k - k_s + i\gamma_{m,s}^{(2)}\right] = -\gamma_{m,s}^{(1)}\gamma_{m,s}^{(2)}\left(t_{2m}\right)^2 \tag{13}$$

which can be solved to give

$$k_{m,1} = \frac{1}{2}\left(k_{m,s}^{(1)} - i\gamma_{m,s}^{(1)} + k_{m,s}^{(2)} - i\gamma_{m,s}^{(2)}\right) + \sqrt{\left(k_{m,s}^{(1)} - i\gamma_{m,s}^{(1)} - k_{m,s}^{(2)} + i\gamma_{m,s}^{(2)}\right)^2 - 4\gamma_{m,s}^{(1)}\gamma_{m,s}^{(2)}\left(t_{2m}\right)^2}$$

$$k_{m,2} = \frac{1}{2}\left(k_{m,s}^{(1)} - i\gamma_{m,s}^{(1)} + k_{m,s}^{(2)} - i\gamma_{m,s}^{(2)}\right) - \sqrt{\left(k_{m,s}^{(1)} - i\gamma_{m,s}^{(1)} - k_{m,s}^{(2)} + i\gamma_{m,s}^{(2)}\right)^2 - 4\gamma_{m,s}^{(1)}\gamma_{m,s}^{(2)}\left(t_{2m}\right)^2} \tag{14}$$

These values are used as initial approximations for each of the two possible solutions. Results of numerical solution of Eq. (11) are shown in Fig. 1
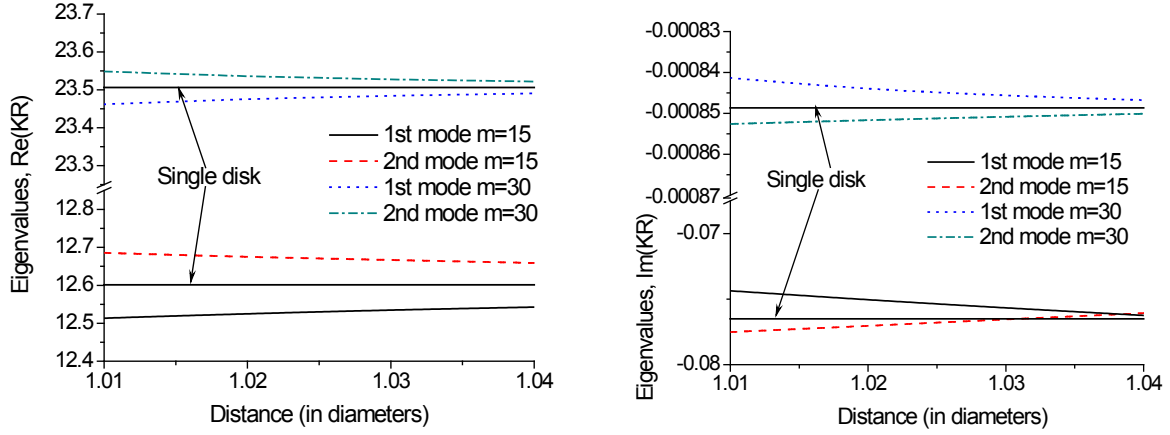
Fig. 1. Dependence of the real (left) and imaginary (right) parts of two modes of the two-coupled disks system on the distance between the disks. Radii, R, of the both disks are the same.

Taking into account the double-degeneracy of the modes of the two-disk system, one can define four linearly independent modes as follows:

$$(1): d_{m,1}^{(1)} = N_{m,1} \tilde{\alpha}_{m,1}^{(1)} \kappa_{m,1}^{(2)} t_{2m}; \, d_{-m,1}^{(2)} = N_{m,1}; \, d_{-m,1}^{(1)} = 0; \, d_{m,1}^{(2)} = 0; \tag{15}$$

$$(2): d_{m,2}^{(1)} = N_{m,2} \tilde{\alpha}_{m,2}^{(1)} \kappa_{m,2}^{(2)} t_{2m}; \, d_{-m,2}^{(2)} = N_{m,2}; \, d_{-m,2}^{(1)} = 0; \, d_{m,2}^{(2)} = 0; \tag{16}$$

$$(3): d_{-m,3}^{(1)} = N_{m,3} \tilde{\alpha}_{m,1}^{(1)} \kappa_{m,1}^{(2)} t_{2m}; \, d_{m,3}^{(2)} = N_{m,3}; \, d_{m,3}^{(1)} = 0; \, d_{-m,3}^{(2)} = 0; \tag{17}$$

$$(4): d_{-m,4}^{(1)} = N_{m,4} \tilde{\alpha}_{m,2}^{(1)} \kappa_{m,2}^{(2)} t_{2m}; \, d_{m,4}^{(2)} = N_{m,4}; \, d_{m,4}^{(1)} = 0; \, d_{-m,4}^{(2)} = 0; \tag{18}$$

where we introduced an abbreviated notation

$$\tilde{\alpha}_{m,i}^{(1,2)} = \tilde{\alpha}_m^{(1,2)}\left(k, k_{m,i}\right); \, \kappa_{m,i}^{(1,2)} = \kappa_m^{(1,2)}\left(k, k_{m,i}\right) \tag{19}$$

The fields in the respective modes are

Mode 1

$$F_{1,1}^{(1)} = R^{-1} N_{m,1} \tilde{\alpha}_{m,1}^{(1)} \kappa_{m,1}^{(2)} H_{2m}\left(n_0 k R_{12}\right) e^{im\varphi} J_m\left(n_d k_{m,1} \left|\mathbf{r} - \mathbf{r}_1\right|\right)$$
$$F_{1,1}^{(2)} = R^{-1} N_{m,1} e^{-im\varphi} J_{-m}\left(n_d k_{m,1} \left|\mathbf{r} - \mathbf{r}_2\right|\right) \tag{20}$$

Mode 2

$$F_{1,2}^{(1)} = R^{-1} N_{m,1} \tilde{\alpha}_{m,1}^{(1)} \kappa_{m,1}^{(2)} H_{2m}\left(n_0 k R_{12}\right) e^{-im\varphi} J_{-m}\left(n_d k_{m,1} \left|\mathbf{r} - \mathbf{r}_1\right|\right)$$
$$F_{1,2}^{(2)} = R^{-1} N_{m,1} e^{im\varphi} J_m\left(n_d k_{m,1} \left|\mathbf{r} - \mathbf{r}_2\right|\right) \tag{21}$$

Mode 3

$$F_{2,1}^{(1)} = R^{-1} N_{m,2} \tilde{\alpha}_{m,2}^{(1)} \kappa_{m,2}^{(2)} H_{2m} \left(n_0 k R_{12} \right) e^{im\varphi} J_m \left(n_d k_{m,2} \left| \mathbf{r} - \mathbf{r}_1 \right| \right)$$

$$F_{2,1}^{(2)} = R^{-1} N_{m,2} e^{-im\varphi} J_{-m} \left(n_d k_{m,2} \left| \mathbf{r} - \mathbf{r}_2 \right| \right) \tag{22}$$

Mode 4

$$F_{2,2}^{(1)} = R^{-1} N_{m,2} \tilde{\alpha}_{m,2}^{(1)} \kappa_{m,2}^{(2)} H_{2m} \left(n_0 k R_{12} \right) e^{-im\varphi} J_{-m} \left(n_d k_{m,2} \left| \mathbf{r} - \mathbf{r}_1 \right| \right)$$

$$F_{2,2}^{(2)} = R^{-1} N_{m,2} e^{im\varphi} J_m \left(n_d k_{m,2} \left| \mathbf{r} - \mathbf{r}_2 \right| \right) \tag{23}$$

where R is characteristic size of the resonators used in the definition of the normalization constants $N_{m,i}$ (see Eq. (28) below). If disks are identical, it is their radius. Now, we need to define the inner product of the modes. To this end we first introduce two-dimensional vectors

$$\left| F_i \right\rangle = \begin{pmatrix} F_i^{(1)} \\ F_i^{(2)} \end{pmatrix} \tag{24}$$

and their adjoints

$$\left\langle F_i \right| = \begin{pmatrix} {}^\dagger F_i^{(1)} & {}^\dagger F_i^{(2)} \end{pmatrix} \tag{25}$$

where :

$$^\dagger F_i^{(k)} \left(r, \varphi \right) = F_i^{(k)} \left(r, -\varphi \right) \tag{26}$$

Now the inner product is defined as

$$\left\langle F_i \middle| F_j \right\rangle = \int_0^{R_1} \int_0^{2\pi} {}^\dagger F_j^{(1)}(r,\varphi) F_i^{(1)}(r,\varphi) r dr d\varphi + \int_0^{R_2} \int_0^{2\pi} {}^\dagger F_j^{(2)}(r,\varphi) F_i^{(2)}(r,\varphi) r dr d\varphi \tag{27}$$

One can prove that the modes introduced in Eq. (20) through Eq. (23) are orthogonal with respect to the inner product defined by Eq. (27). Normalization of the modes is defined by the following normalization condition

$$2\pi \left[N_{m,i} \right]^2 \left\{ \left[\tilde{\alpha}_m^{(1)}(k, k_{m,i}) \kappa_{m,i}^{(2)} H_{2m} \left(n_0 k R_{12} \right) \right]^2 \right.$$

$$\left. \times \upsilon_1^2 \int_0^1 \left[J_m \left(n_d k_{m,i} R_1 \rho \right) \right]^2 \rho d\rho + \upsilon_2^2 \int_0^1 \left[J_m \left(n_d k_{m,i} R_2 \rho \right) \right]^2 \rho d\rho \right\} = 1, \tag{28}$$

where $\upsilon_1 = R_1 / R; \upsilon_2 = R_2 / R$

2.1.2 Lasing equations and analysis of single mode operation

The relatively low Q-factor of the coupled disk system and the presence of degenerate modes make standard lasing rate equations unsuitable for modeling the structure under consideration. Therefore, parts of our efforts were devoted to derivation of the system of equations for amplitudes of lasing modes. For details on the derivation of the lasing equations, please see the **appendix**. These equations were used to analyze the single mode operation of the double disk laser as well as compute coefficients of nonlinear inter-mode coupling, which are essential for determination of the system parameters suitable for the bistable behavior. The

Fig. 2 Dependence of the single mode lasing frequency and threshold for two modes, as functions of the QD frequency for two inter-disk distances, *d*, measured in disk's diameter.

results of our modeling are shown in Fig. 2. The lasing frequencies of the two non-degenerate modes as functions of the frequency of quantum dot (QD) transition in the regime when only one of the modes is assumed to attain lasing is shown in Fig. 2(a). Figure 2(b) presents dependence of the single mode lasing threshold for the same two modes also as functions of QD frequency.
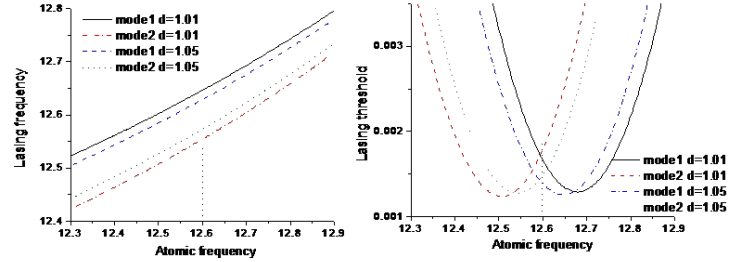
2.1.3 Finite Difference Time Domain Simulation of Coupled Microring Resonator
We performed finite difference time domain simulations of the coupled microrings and established the mode splitting that happens in these resonators. Transmission spectra at the two ports are shown in Fig. 3 clearly showing the mode splitting. Also shown in Fig. 3 is the electric field distribution in the coupled ring resonator system at the resonances.
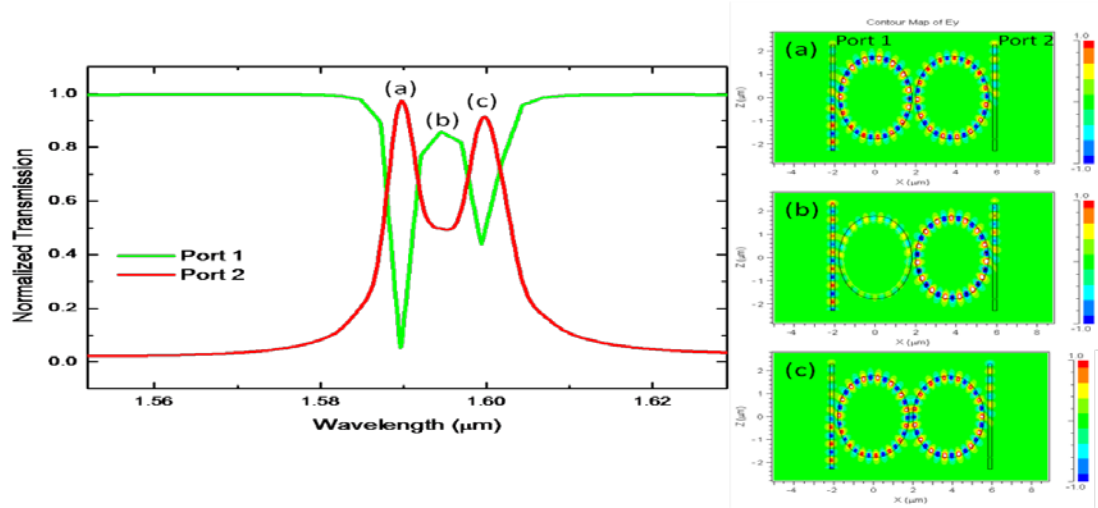

Fig. 3. Transmission characteristics of the coupled microring resonator showing the splitting of modes. Also showin on the right are the electric field profiles in the coupled resonators at the three spectral positions (a), (b) and (c).

2.2 Fabrication of Active Micro-resonators

2.2.1 Dielectric Microdisks with Quantum Dots

On the experimental front, we fabricated active and passive microdisks. Although we had originally proposed to use SU8 as the host medium to embed the colloidal quantum dots to realize the active disks, the QC team recently introduced SiNx as a host matrix with a significant advantage of having very small detrimental effect on the luminescence properties of the embedded dots. Schematic drawing of the active microdisk is shown in Fig. 4. The SiNx disk is fabricated on a SiO2 buffer layer which acts as the low index bottom cladding layer as

Fig. 4. Schematic drawing of the active microdisks realizing using colloidal quantum dots embedded in a SiNx host.

well. The SiNx disks vary in diameter (5 µm to 20 µm) and are 0.5 µm thick. The entire structure is realized on Si substrate and grown using a combination of plasma enhanced chemical vapor deposition and spin coating.
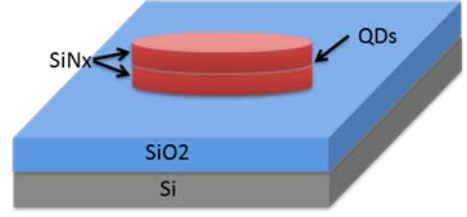
Following the deposition of the different layers in the following order: SiO2, SiNx, QDs, SiNx, the microdisks are patterned using electron beam lithography using PMMA as the electron beam resist. The patterned PMMA is then used as the etch mask to etch the microdisks onto the SiNx layer using reactive ion etching. Scanning electron microscope images of coupled passive disks and single active disks are show in Fig. 5. CdSe colloidal QD with emission maximum at 600 nm wavelength was used as the active component in these disks. These QDs were deposited using spin coating. It was observed

Fig. 5. SEM image of active microdisk embedded with red emitting CdSe colloidal quantum dots (left) and coupled microdisks with 500 nm spacing (right).

that the sidewalls of the microdisks fabricated using the above technique suffered from significant sidewall roughness which in turn affected the luminescence properties.
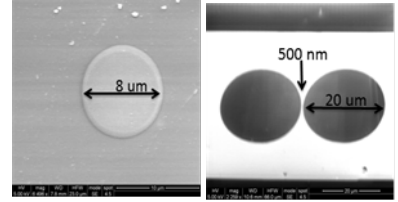
Focused ion beam etching was explored as an alternate technique to realize smooth sidewalls for the microdisks. This was carried out at Brookhaven National Labs – Center for Functional Nanomaterials (Fig. 6).
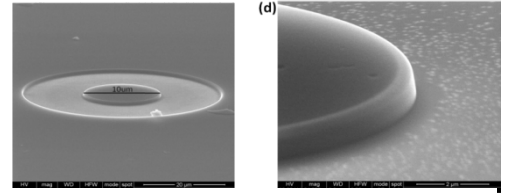

Fig. 6. SEM image of active microdisks patterned using focused ion beam etching. As can been seen, the sidewalls are far soother than disks patterned using RIE,

2.2.2 Polymer microdisk/rings

In addition to the all-dielectric microdisks, we have also investigated single and coupled microdisk/ring structures embedded with colloidal CdSe quantum dots and Rhodamine 6G organic dye. The choice of this dye was motivated by the high photostability
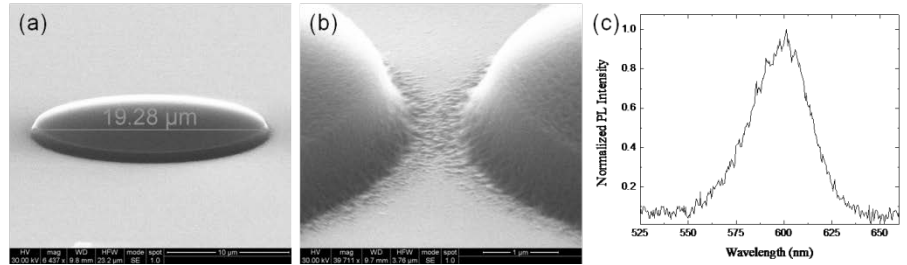

Fig. 7. (a) SEM image of polymer microdisks embedded with Rhodamine 6G. **(b)** Sidewall images of a coupled disk system and **(c)** Photoluminescence spectra collected from the microdisk resonator.

and high quantum yield (0.95). This approach provides an alternate approach for realizing low-cost microlasers. The high quantum yield of the dye as compared to the colloidal QDs was the primary motivation for pursuing this approach. We expect the dye doped material to exhibit lasing at lower thresholds than the quantum dot system. The dye was dissolved along with SU8 (Microchem Inc.) and thinned using a thinner to obtain one micron thick films. The dye doped films were later patterned using either EBL or photolithography. Scanning electron microscope images of the dye doped disks fabricated in SU8 is shown in Fig. 7 along with the emission obtained. Once again we see the surface roughness of the microdisks to be a hindrance in observing the WGMs. It should however be noted that in both the dye doped samples as well as in the QD embedded disk samples, light was collected in the far-field and this often deteriorates the signal integrity. A side out-coupling geometry is currently being designed to enhance the coupling.

We fabricated Rhodamine 6G infiltrated polymer microrings using the same fabrication protocol established for the microdisk resonators. Scanning electron microscope images of single and coupled microring resonators fabricated using EBL are shown in Fig. 8. Far-field emission measurements showed very weak PL signal since the amount of dye in the rings is far smaller than that in the disks. As a natural direction in this project, we are now developing structures with waveguides coupled to the rings.
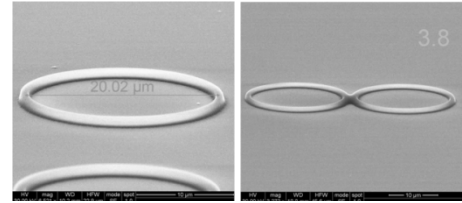

Fig. 8. SEM images of single and coupled microring resonators infiltrated with Rhodamine 6G.

A vertical coupling geometry was used to fabricate the passive waveguides coupled to the active microrings. Schematic of the flow diagram for fabricating the structure is shown in Fig. 9. The passive waveguides were fabricated at QC-CUNY using electron beam lithography. This was followed by the deposition of a top cladding layer of silicon dioxide, the thickness of which determines the coupling between the passive waveguides and the ring. Finally active microrings were defined on our standard silicon nitride structure embedded with QDs or dye using FIB technique at Brookhaven. The major fabrication issue we had in this context was the precise alignment of the passive and active waveguides.
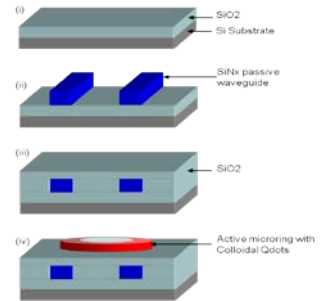

Fig. 9. Schematic flow diagram for the fabrication of the vertically coupled microring system.

2.2.3 Vertical coupled microcavities

Recently Menon's group at QC-CUNY has developed a fabrication protocol that uses plasma enhanced chemical vapor deposition (PECVD) compatible with colloidal quantum dots without deteriorating the optical properties of the dots. In the present program that approach has been utilized to develop coupled vertical microcavities to realize bistable lasing. The entire cavity structure is fabricated using PECVD and the quantum dot layers are deposited via spin coating or dip-coating. Shown in Fig. 10 is the schematic of the coupled vertical microcavity structure. The number of periods of the middle DBR was controlled to manipulate the coupling between the microcavities.

Fig. 10. Schematic of a coupled microcavity.

Fabrication

Using a combination of nitrous oxide, silane, and ammonia, we deposit layers of silicon oxide (SiO_2) and silicon nitride (Si_3N_4). Plasma enhanced chemical vapor deposition is used for the growth of these dielectric layers. The SiO_2 and Si_3N_4 layers are estimated to have refractive indices of 1.45 and 1.77, respectively. A low temperature growth technique was developed to deposit the dielectric layers on top of the active QDs to avoid the QDs from getting affected due to the growth process. This was an important process development in the program since it established the protocol to introduce active material between dielectric layers without having detrimental effect on the optical properties of the QDs.

Characterization and Modeling

By controlling the number of periods of the middle DBR, one can control the field distribution in the coupled microcavities. Additionally, the reflectivity and transmission spectrum shows the split modes arising due to the interaction between the microcavities as seen in Fig. 11. The top panel of Fig. 11 shows the split modes arising when the number of intermediate DBR periods is small (3.5) and the bottom panel shows the reflectivity spectrum showing lesser splitting of the modes since the number of intermediate DBR periods is larger (10.5). The former case corresponds to strong interaction between the two cavities. The experimentally obtained reflectivity data is compared to simulations based n transfer matrix method. The corresponding electromagnetic field profiles are shown in the right panel of Fig. 11. As can be seen, it is possible to precisely control the field distribution in these coupled resonator systems by engineering their coupling strengths. The electromagnetic field simulations were also carried out using transfer matrix method. Following this we carried out time resolved and steady state photoluminescence measurements on the emission characteristics of the QDs embedded in the coupled microcavity structures (Fig. 12). A Purcell enhancement of 2.5 was observed for the system of coupled cavities embedded with CdSe QDs in one of the cavities.
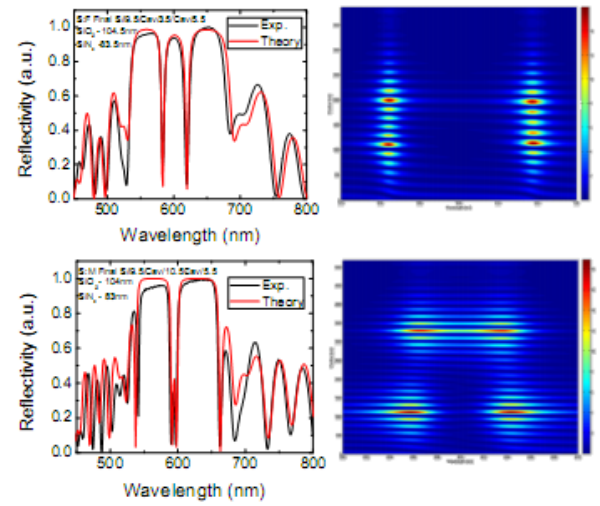

Fig. 11. Coupled microcavities reflectivity with fitted spectra, side-by with electric field intensity profile. Separations between the two cavities are 3.5, and 10.5 periods for top, and bottom graphs respectively. The field intensity is represented by the color, vertical and horizontal axis, are position within the structure and wavelength, respectively.
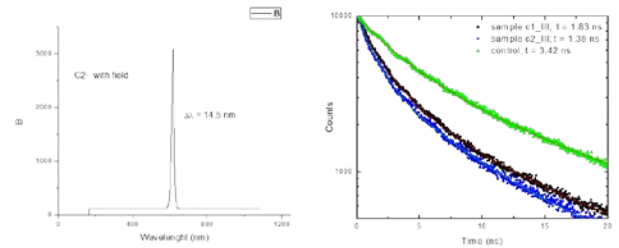

Fig. 12. Photoluminescence (PL) from QDs in coupled microcavity. (Left) Steady state and (Right) Time resolved PL.

3. Single Resonator System

3.1 Theory of linear bistability mechanism

Significant efforts have been devoted this year to exploring a new type of optic bistability in lasers, which does not rely on mode competition or saturable absorbers, and is expected,

therefore, to show bistable behavior at lower power consumptions and with faster switching times. This mechanism of bistability is realized in structures shown in Fig. 13, where two active waveguides (length of active portion L) are coupled to each other via a disk or ring resonator (circumference L_r, refractive index n_r). The feedback necessary for lasing is provided in this structure by combination of two factors: mirrors at one end of each waveguide and coupling of the waveguides via the resonator, which redirect optical signal reflected from one waveguide mirrors to another waveguide closing the loop. Normal modes of this structure are defined by the following equations for the real parts of the propagating constants in the waveguides, $q_m^{(1,2)}$
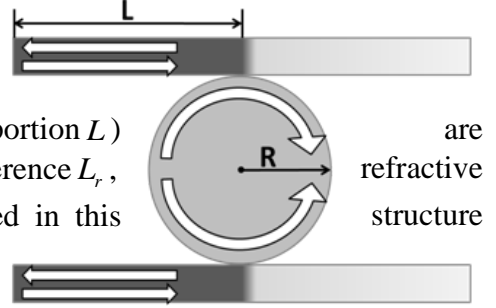

Fig. 13. A schematic of the structure suggested for realization of the linear bistability mechanism

$$\left(q_m^{(1)} + q_m^{(2)}\right)L = \pi m \tag{29}$$

and their imaginary parts $\delta_m^{(1,2)}$

$$\left(\delta_m^{(1)} + \delta_m^{(2)}\right)L = -\frac{1}{2}\ln S(\omega)$$

Eq. (29) indicates that the disk does not affect the modal structure of the system, which is similar to that of an effective Fabry-Perot resonator of length $2L$. Its role is to determine the modal losses, characterized by $\delta_m^{(1,2)}$, via resonator form-factor $S(\omega)$ defined as

$$S = \frac{\alpha^2 r^2 |\kappa|^4}{1 + \alpha^4 |p|^4 - 2\alpha^2 |p|^2 \cos\left(2\pi\frac{\omega}{\omega_r}\right)}$$

where $\omega_r = (2\pi c)/(n_r L_r)$ (c is speed of light in vacuum), α^2 describes round-trip losses in the resonator, p and κ are coupling parameters obeying $|p|^2 + |\kappa|^2 = 1$. The resonator also introduces a phase shift between the fields in the waveguides defined by

$$\psi = \Phi/2 - \tan^{-1}\frac{|p|^2 \alpha \sin\Phi}{1 - |p|^2 \alpha \cos\Phi} \tag{30}$$

where $\Phi = n_r \omega L_r / c$.

We confirmed these conclusions about the modes of our structure by direct numerical simulation of the waveguide-resonator system using COMSOL simulation platform. The results of the simulations showing the structure of the modes is shown in Fig.14.

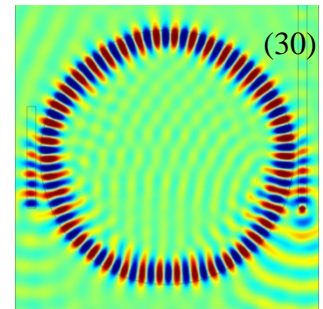Using found modes we developed a theory of a single-mode lasing in

Fig. 14 Field distribution in a coupled waveguide-resonator structure in one of its modes.

this structure. According to the theory, the stationary lasing frequency, Ω and respective intensity I are defined by the system of equations

$$\Omega - \nu = P\Omega g\left(\Omega\right)\left[\frac{\omega_0 - \Omega}{\gamma_\perp}F_1(I,\Omega) - F_2(I,\Omega)\right]$$

$$\ln S\left(\Omega\right) = -2\pi\frac{P\Omega g\left(\Omega\right)}{\omega_B}\left[F_1(I,\Omega) + \frac{\omega_0 - \Omega}{\gamma_\perp}F_2(I,\Omega)\right]$$

(31)

where ν is the frequency of the "cold" cavity mode, ω_0 and $\gamma_\perp$ are the frequency and the linewidth of the lasing atomic transition, $g\left(\Omega\right)$ is the gain Lorentzian, P is pumping rate, and $F_{1,2}(I,\Omega)$ are integrals of the modal functions $U\left(z\right)$

$$F_1(I,\Omega) = \mathrm{Re}\left(\frac{1}{N}\int_0^{2L}\frac{U(z)\bar{U}^*(z)}{1+R}dz\right)$$

$$F_2(I,\Omega) = \mathrm{Im}\left(\frac{1}{N}\int_0^{2L}\frac{U(z)\bar{U}^*(z)}{1+R}dz\right)$$

(32)

taking into account gain saturation through saturation parameter $R = I\left|U(z)\right|^2 g(\Omega)$ (N is mode normalization parameter). We established that under certain conditions controllable by the design of the structure, Eqs. (3.1.2) have multiple solutions, and can, therefore, demonstrate multistable behavior. Stability of these solutions, which are shown in Figure 15 for different pumping levels, depends on P. The behavior of the system is characterized by three threshold values of pumping power $P_1 < P_2 < P_3$ Below the lowest one no lasing takes place, for $P_1 < P < P_2$ one has a standard single-mode laser. However, when $P_2 < P < P_3$ the non-lasing solution becomes one of two stable solutions so that depending on initial conditions the system can either laze or not. This regime is ideal for developing an optical logic element, in which lasing regime would correspond to 1 and non-lazing to zero. The switching between the regimes can be realized using injection locking of the initial frequency. Further increase of the pumping results in the zero intensity solution losing its stability. However, in its place another lasing solution with a frequency and intensity different from the first one becomes stable, so that now one has two stable lasing solutions characterized by different frequencies and intensities. The bistability discussed here is not characterized by a typical hysteresis-like dependence of intensity versus pumping, which is typical for other types of bistability.
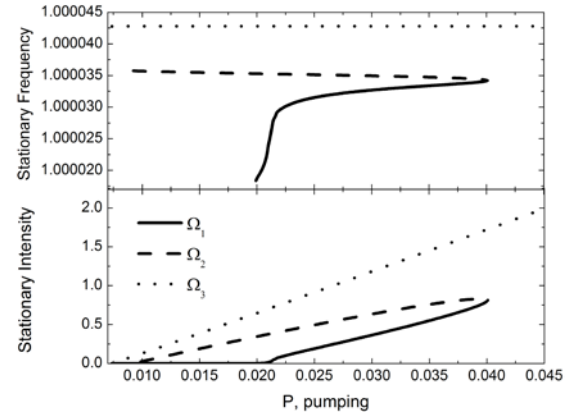

Fig. 15. (a) Dependence of stationary lasing frequency and intensity on pump power and (b) Temporal evolution of lasing frequency and intensity

3.2 Fabrication of active/passive integrated waveguides

We fabricated colloidal QD embedded waveguides to study the transmission losses. The waveguides were fabricated using CdSe colloidal quantum dots dispersed in SU8. The patterning was done using electron beam lithography. Figure 15 shows SEM images of one such waveguide embedded with CdSe/ZnS core/shell quantum dots emitting at 600 nm. The L-shaped quantum dot embedded waveguide was optically excited using an Ar-ion laser (λ= 488 nm) from one of the ends and the emission from the

Fig. 16. Top panel shows SEM images of active-passive integrated polymer waveguides. The active waveguides consist of CdSe quantum dots dispersed in SU8. Bottom panel shows CCD images of optical pumping experiment clearly demonstrating waveguiding and minimal scattering from due to clustering of quantum dots.

quantum dots was found to be clearly waveguiding. Based on the CCD image (Fig. 15 bottom panel) it can be concluded that the scattering induced loss is very minimal as we do not see much scattered light from the side walls. Most of the light emission is observed from the ends indicating good waveguiding. Furthermore, the waveguides did not show much losses at the bends. This is a very promising result towards realizing active photonic structures using colloidal quantum dots which can be integrated with passive structures.
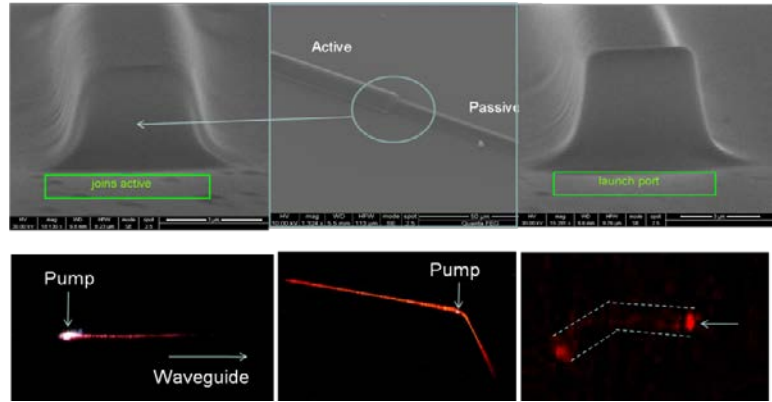
4. Enhanced Gain from QDs in Microcavity

Using a combination of PECVD and dip coating, we fabricated one-dimensional microcavity structures as shown schematically in Fig. 17.

The dielectric layers of the MC structure were fabricated using plasma enhanced chemical vapor deposition (PECVD). The MC consists of two distributed Bragg reflectors (DBRs) separated by a thin layer of CdSe/ZnS (core/shell) QDs. The DBRs consisted of alternating layers SiO_2 and

Si_3N_4. The bottom DBR consisted of 10 pairs of Si_3N_4/SiO_2 deposited on a glass substrate. The cavity layer consisting of a QD film was then deposited by dip coating in a solution of QDs in toluene of 10 mg/ml concentration, and pulled at a rate of 1 mm/min. The resulting film was estimated to be ~200 nm thick. The top DBR consisting of 9 pairs was then deposited on top of the QD layer (schematic shown in the inset of Fig. 1). The reflectivity spectrum of the resulting MC at normal incidence was measured using a tungsten-halogen light source coupled to a CCD based spectrometer via an optical fiber. The reflectivity spectrum consists of a stopband with a transmission window centered at 630nm and a full-width-half-maximum
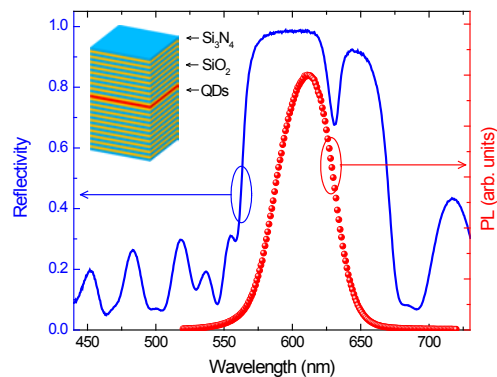
Fig. 17 (Inset) Schematic of the MC structure. The normal incidence reflectivity of the MC is plotted together with the PL spectrum of a solution of QDs in toluene.

(FWHM) of ~10 nm, which spectrally overlaps with the photoluminescence (PL) spectrum of the QDs, as shown in Fig. 17. A control sample consisting of a QD layer film between two SiO$_2$ layers was used for comparison.

Steady-state PL was used to determine the effects of the cavity on the QDs. The QDs were optically pumped with a continuous-wave (CW) argon-ion laser, and the spectra were collected using a fiber-coupled CCD based spectrometer. The FWHM of the PL narrows to 10 nm compared to the control sample linewidth of 32 nm, as shown in Fig. 18a.

The PL peak wavelength of the MC is slightly red-shifted compared to the control sample due to the cavity resonance being at a higher wavelength than then bare QDs (see Fig. 17). We observe the PL is cavity linewidth limited (10 nm) and peak is spectrally located at the cavity resonance (~625 nm, see Fig. 17) indicating the QD emission is coupled to the cavity mode. To demonstrate enhancement of PL, optical power dependent measurements were performed. The PL intensities for the MC is higher than the control for all powers measured, however, no threshold behavior is observed (see Fig. 18b).

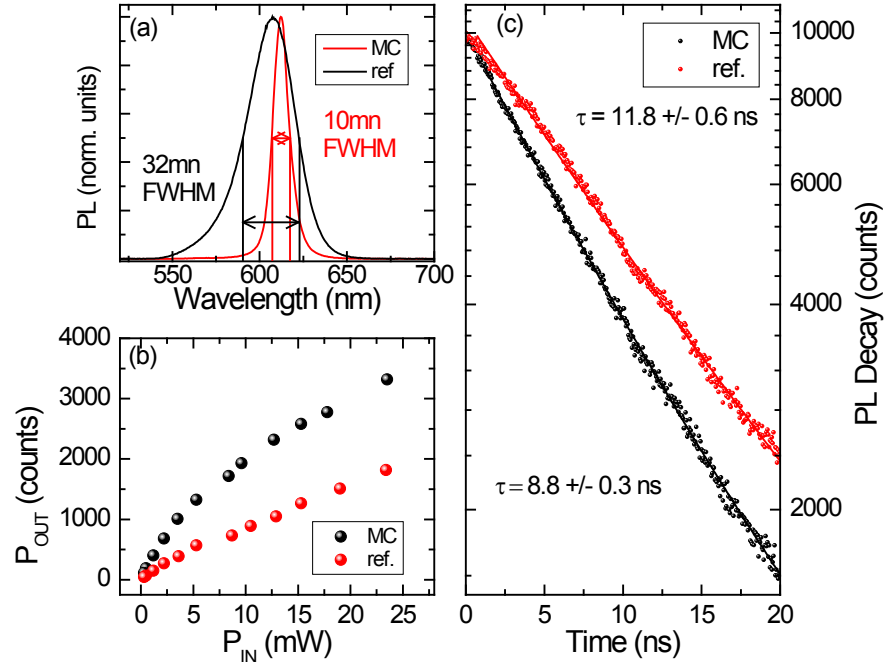Furthermore, time-resolve PL was carried out to determine the

Fig. 18. (a) Normalized PL for the MC and control sample. The PL of the MC sample is narrower (10 nm FWHM) than the control (32 nm FWHM). (b) Power dependent PL peak intensities show the MC structure has greater intensity than the control sample. (c) Time-resolved PL measurements are plotted for the control (red) and MC (black) sample.

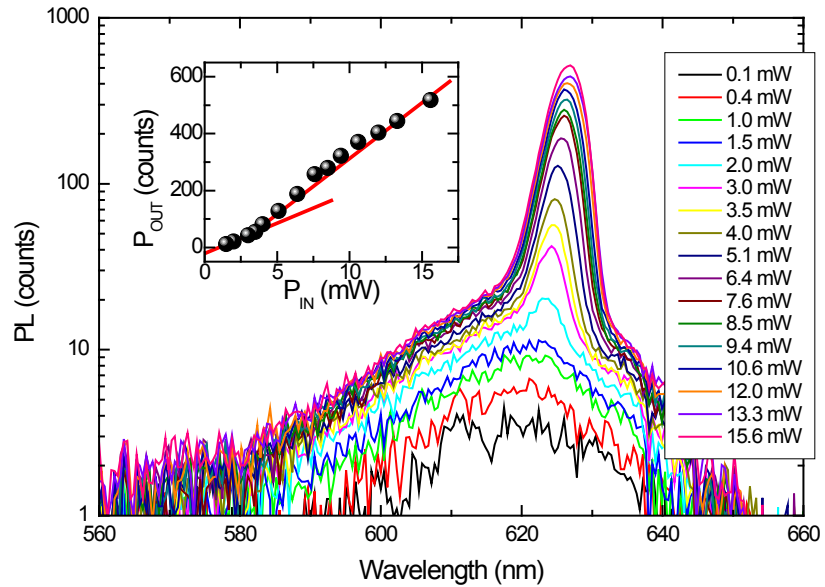
Fig. 19.. (a) PL spectra for pump powers varying from 0.1 mW to 15.5 mW. The biexciton peak begins to appear with 2.0 mW pump power. (b) The biexciton peak power is plotted against the time-averaged input power to show the threshold behavior.

radiative lifetime of the QDs confined in the MC. To this end, a time-correlated single photon counting technique using a pulsed 467 nm, < 200 ps pulsewidth laser was used. The lifetime of the QDs in the MC was found to be 8.9 ±0.3 ns, while the control sample was measured to be 11.8 ± 0.6 ns. The MC structure yielded a Purcell factor ~1.3. The time-resolve PL is shown in Fig. 18c.

Power dependent PL measurements were repeated at higher intensities using the second harmonic (532 nm) of a Nd:YAG laser. Amplified spontaneous emission (ASE) of the biexcitons begin to appear at a power of 2.0 mW, as shown in Fig. 19(a). The PL intensity of the biexcitons exhibit a threshold behavior which is shown in Fig. 19(b). The angular dispersion allows for tuning the cavity mode to be in resonance with the ASE peak by changing the collection angle. Furthermore,

Fig. 20. (a) PL emission pattern of biexciton ASE in MC. The emission is highly directional when compared to the Lambertian emission pattern. (b) The gain of the biexcitons is enhanced when in resonance with the microcavity.

angle dependent PL show the effects of angular dispersion of the MC mode. The biexciton PL is in resonance with the cavity at a 5◦ angle to the normal. The enhancement of the gain of the biexcitons is clearly seen from the increase PL intensity at resonance (Fig. 20(b)). This effect yield highly direction emission when compared to the Lambertian pattern as shown in 20(a).
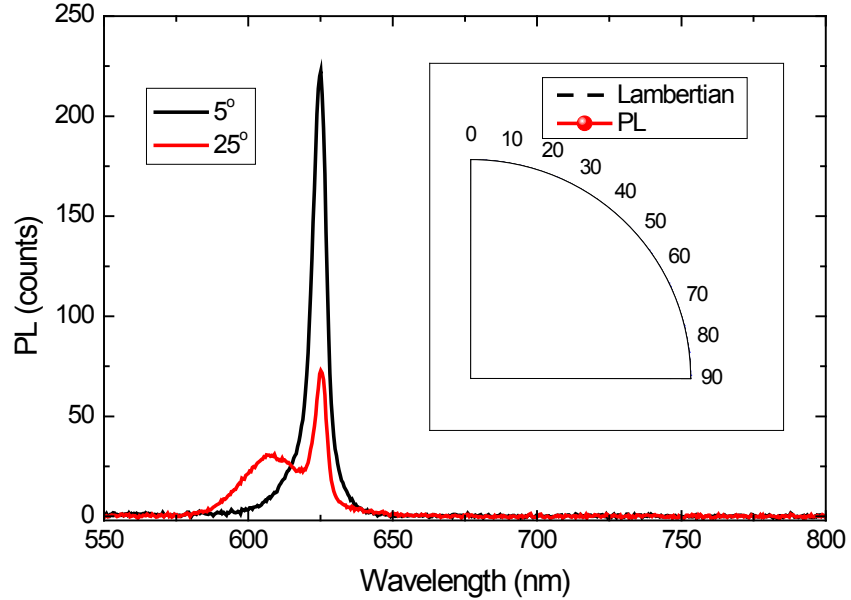
This work demonstrates the enhancement of gain in an all-dielectric MC. Time-correlated single-photon counting technique was used to measure increase of 33% in the radiative rate of the QDs inside the MC. Spectroscopic measurements show the enhanced PL power of the QDs in the MC compared to the control sample. Pumping at higher powers enhance the gain of the biexcitons. The enhancement of light-matter interaction is such system can be further developed into and have implications in low cost optically active devices.

5. Gain measurements using variable stripe length measurements

To better understand the gain characteristics of the CdSe QDs used in the device demonstrations discussed above we carried out gain measurements using the variable stripe length technique. Here, the NdYAG laser was focused down to the sample using a cylindrical lens and the stripe length was determined using a beam blocker with a micrometer attached to it to vary the stripe length. The QDs were deposited using dip coasting technique similar to the MC structures
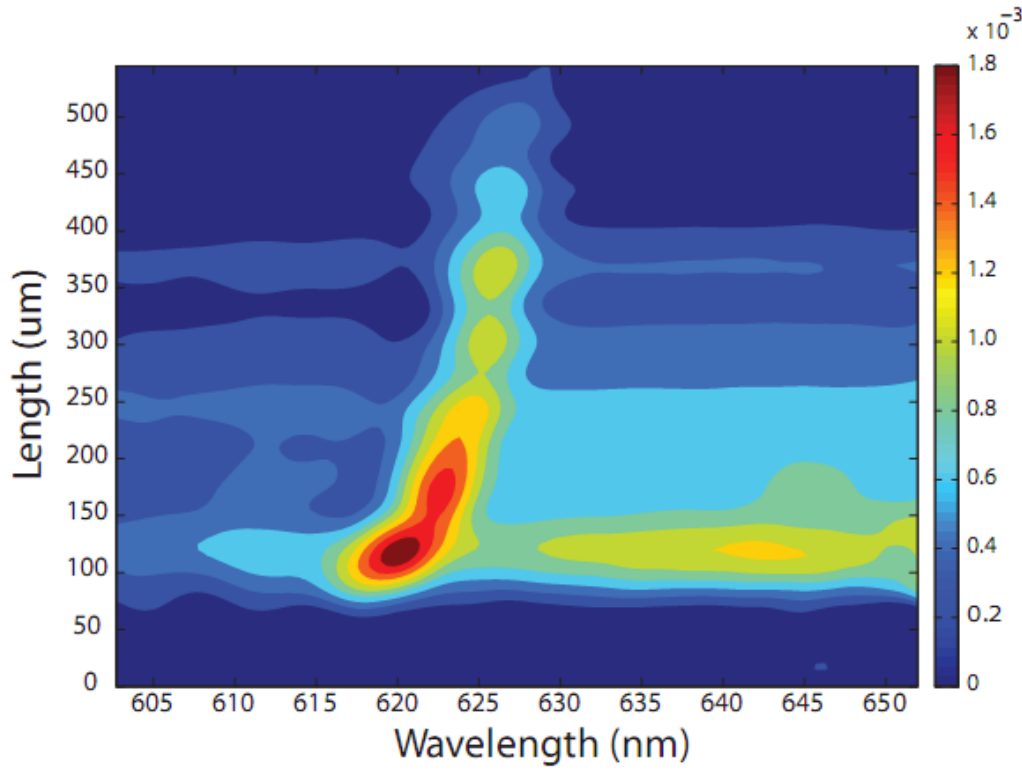
Fig. 21 Results of variable stripe length measurements carried out on the CdSe QDs
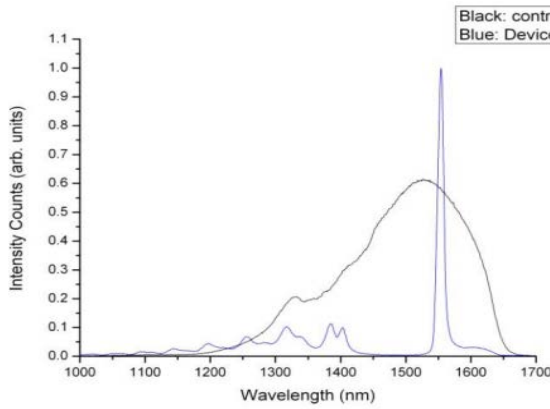

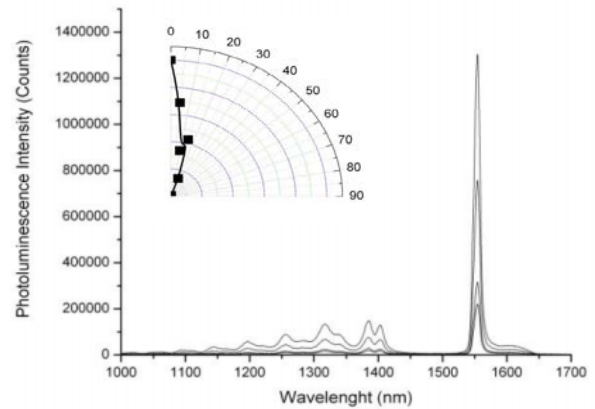**Fig. 22** Steady state PL measurements showing significant spectral narrowing inside the microcavity.

Fig. 23 Power dependence of PL emission. The inset shows the directionality in emission.

discussed above. The gain spectrum was measured for different stripe lengths and the result obtained is shown in Fig. 21. The maximum gain observed was ~ 1.8 x 10^{-3} μm^{-1}.

Similar devices were also fabricated using PbSe QDs emitting in the 1550 nm wavelength range. The MC was once again fabricated via PECVD and the QDs were deposited via spin coating. Results of the near IR emitting microcavity device is shown in Fig. 22. It is clearly seen that the emission spectrum narrows considerably when the QDs are embedded in the MC. Although gain was not observed in these QDs, we do see clear evidence of enhancement of spontaneous emission due to the Purcell effect (Fig. 22). The power dependent spectrum is shown in Fig. 23. The inset of Fig. 23 shows the directionality in emission observed from the PbSe QDs clearly indicating coupling of the emission into the cavity mode.

6. Bistability in nonlinear grating

We have looked into the possibility of observing bistability using a grating structure for feedback. A schematic of the lasing structure based on a distributed feedback geometry is shown in Fig. 22.

Calculations are carried out for small-signal amplification. In the small-signal regime, the optical power is too small to affect the gain value. Amplifier gain $G = I_{out}/I_{in}$ is calculated for a $\lambda/4$ phase shifted DFB. A schematic of the such an experiment is depicted in figure 1.

The parameters used were $\kappa L = 0$, $\alpha_{int} L = 0$. Figure 23 shows the wavelength dependence of the amplifier gain for different modal gain powers and for different values of α. The spectral shift can be understood by increasing the gain results in a decrease in refractive index. Therefore, the transmission shifts to higher values.

Nonlinearities exist in all gain media as gain saturation occurs in the large-signal regime and a nonlinear change in the refractive index occurs along with it. This nonlinearity, together with, the feedback mechanism, can produce regions of bistability.

In order to incorporate these effects into the calculations, an intensity dependent gain of the form $g = g_0/(1+I/I_{sat})$ is used. Since the transfer matrix method uses g to calculate the intensity, a self-consistent approach is need. The approach taken is to use a first order approximation $g = g_0$, and calculate the intensity distribution. Using the calculated intensity distribution, a new value of g is calculated. Now using this value of g, the
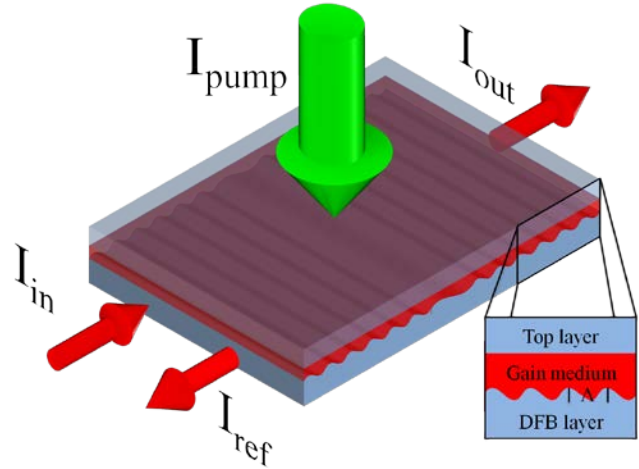

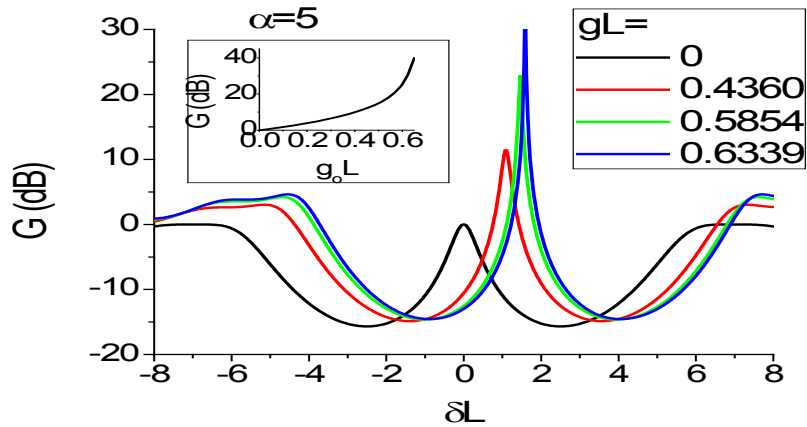**Fig. 22.** Top panel: Schematic of the grating based bistability scheme.

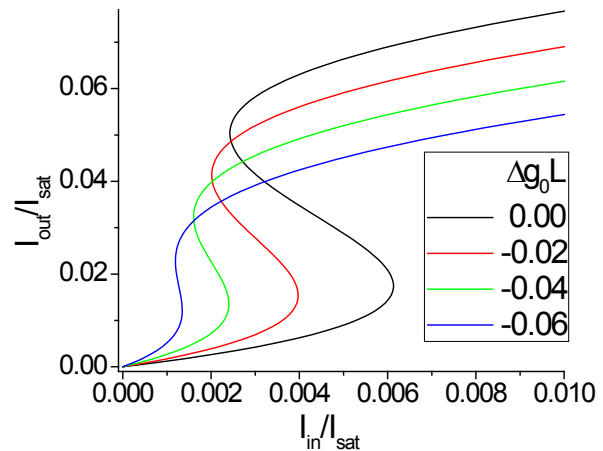**Fig. 23** Gain dependence on wavelength.

Fig. 24. Bistability curves for different gain values

intensity distribution is again calculated. This process is repeated until the intensity distribution converges.

Bistability exists for wavelengths higher than the transmission peak. Hysteresis curves are plotted for values of δL in the vicinity of the onset of bisability ($\delta L = 1.5$). Based on realistic estimates of gain coefficient of colloidal QDs and the typical device length (500 microns – 1000 microns), we estimated the threshold power levels to be in mW range which can be easily obtained.

We also carried out pump power dependent measurements on QDs spin coated on gratings that were fabricated via soft lithography. SEM images of gratings fabricated using electron beam lithography are shown in Fig. 25. The ASE measurements were carried out on gratings fabricated
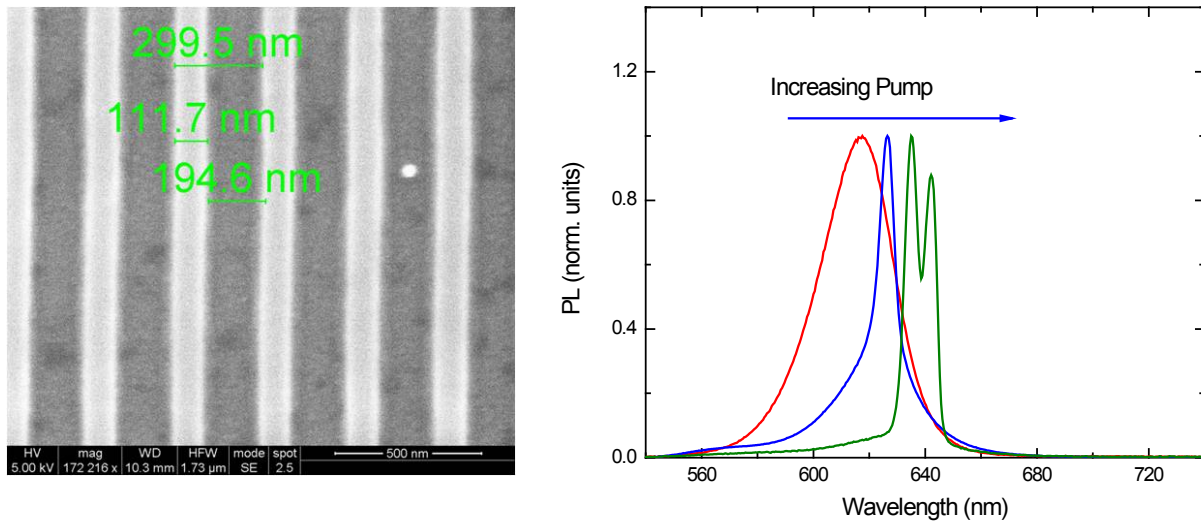
Fig. 25. Scanning electron microscope image of the gratings fabricated on PMMA using electron beam lithography and (b) amplified spontaneous emission from CdSe quantum dots deposited on top of a grating. At high pump power levels, multimode ASE spectrum is observed.

using softlithography. Here we see evidence of the different modes arising due to the feedback from the underlying grating modes.

The final phase of the project was dedicated to the fabrication ogf low cost DFB lasers. This was carried out by taking a commercial DVD and stamping PDMS onto it and creating a negative mould. This was later transferred onto SiO2 via dry etching. Colloidal CdSe QDs were deposited onto the SiO2 gratings via dip coating. An atomic Force Microscope image of the grating is shown in Fig. 26.

Fig. 26. AFM image of grating etched onto SiO2.

The samples were pumped using the NdYAG laser and the observed spectra is shown in Fig. 27(a) along with the power dependence in Fig. 27(b). There is significant spectral narrowing (< 1 nm). The Pout versus Pin graph also shows a clear threshold behavior. We are currently carrying

out coherence measurements to establish that this is indeed a laser and not amplified spontaneous emission.

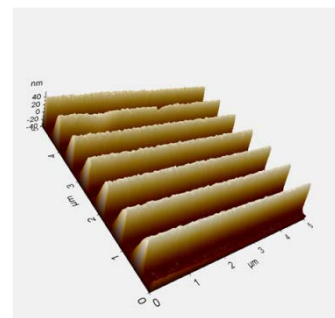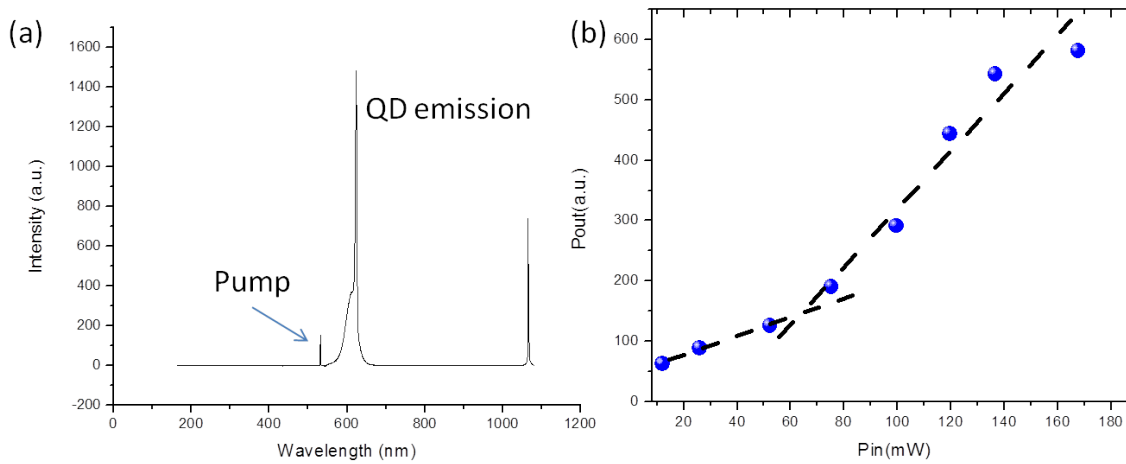**Fig. 27.** (a) Emission spectrum of the QDs coated on the DFB structure fabricated via soft-lithography showing significant spectral narrowing (<1nm). (b) Power dependence of the emission showing clear threshold behavior.

5. Related Publications and Presentations

[1] "A linear bistability mechanism in single-mode lasers," V, Suyavey et. al, Submitted Journal of Optical Society of America A.

[2] "A coupled waveguide – resonator structure exhibiting a new mechanism of lasing bistability and an optical flip-flop device based on it," Deych, Shuvayev, Menon and Lisyansky – Patent Pending.

[3] "Colloidal quantum dot based photonic devices," V. M. Menon, IEEE Winter Topical, Keystone, CO, Jan 2011 (Invited Talk)

[4] "Enhanced gain from colloidal QDs in all-dielectric microcavities," D. Goldberg, and V. M. Menon, IEEE MEMS – NanoPhotonics Conference, 6-9 August 2012, Banff, Canada.

[5] "Enhanced gain from colloidal quantum dots in microcavity," D. Goldberg and V. M. Menon, Submitted – Applied Physics Letters.

[6] "Spontaneous emission enhancement from near infrared emitting PbSe quantum dots in a one-dimensional microcavity," N. Okoye, and V. M. Menon – In Preparation.

APPENDIX

Lasing equations and analysis of single mode operation

In order to derive lasing equations for the structure under consideration we expand the field in the two-disk system in terms of the modes defined in Eq. (20) - (23) and use the orthogonality condition, Eq. (27) to derive equations for slow amplitudes.

We will describe the field and the modes as two-dimensional vectors defined in Eq. (24), and present the modal expansion in the form

$$|E\rangle = \sum_i \sum_{p=1}^{2} \mathrm{E}_{i,p}(\omega)|F_{i,p}\rangle \tag{33}$$

where first index goes over non-degenerate modes, and the second index sums over degenerate ones. Using definition of the adjoint vectors given in Eq. (25) and orthogonality we derive

$$\left(k^2 - k_{m,i}^2\right)\mathrm{E}_{i,p}(k) = -\frac{4\pi k^2}{n_d^2}\langle F_{i,p}|P\rangle =$$
$$-\frac{4\pi k^2}{n_d^2}\left(\iint_{D_1} d\mathbf{r}^\dagger F_{i,p}^{(1)}(\mathbf{r})P^{(1)}(\mathbf{r}) + \iint_{D_2} d\mathbf{r}^\dagger F_{i,p}^{(2)}(\mathbf{r})P^{(2)}(\mathbf{r})\right) \tag{34}$$

where

$$|P\rangle = \begin{pmatrix} P^{(1)} \\ P^{(2)} \end{pmatrix} \tag{35}$$

represent nonlinear polarization due to the gain medium. Introducing slow changing amplitude approximation, we have instead of (34)

$$\left(-k + k_{m,i}\right)\mathrm{E}_{i,p}(k) = \frac{2\pi k}{n_d^2}\left(\iint_{D_1} d\mathbf{r}^\dagger F_{i,p}^{(1)}(\mathbf{r})P^{(1)}(\mathbf{r}) + \iint_{D_2} d\mathbf{r}^\dagger F_{i,p}^{(2)}(\mathbf{r})P^{(2)}(\mathbf{r})\right) \tag{36}$$

We will assume that there are two lasing modes, labeled by index $i = 1, 2$, characterized by frequencies K_i and spatial distribution functions. The latter are comprised of two degenerate modes corresponding to each value of index i:

$$|E_i\rangle = \sum_{p=1}^{2} \mathrm{E}_{i,p}(K_i)|F_{i,p}\rangle\delta(k - K_i) \tag{37}$$

The total field is presented as

$$|E\rangle = \pi\sum_i |\mathrm{E}_i(k)\rangle\delta(k - K_i) \tag{38}$$

Now we follow Ref. [4]. For a given lasing mode i the polarization term in Eq. (36) can be presented in the following form

$$\frac{2\pi k}{n_d^2}\left(\iint_{D_1} d\mathbf{r}\,^\dagger F_{i,p}^{(1)}(\mathbf{r})P^{(1)}(\mathbf{r}) + \iint_{D_2} d\mathbf{r}\,^\dagger F_{i,p}^{(2)}(\mathbf{r})P^{(2)}(\mathbf{r})\right) = \sum_{p_1}\left(V_{ip,ip_1}^{(1)} + V_{ip,ip_1}^{(2)}\right)\mathrm{E}_{ip_1} \tag{39}$$

where

$$V_{ip,ip_1}^{(1,2)} = \frac{2\pi k}{n_d^2}\iint_{D_1}{}^\dagger F_{i,p}^{(1,2)}(\mathbf{r})F_{i,p_1}^{(1,2)}(\mathbf{r})\eta_i^{(1,2)}(\mathbf{r},t)d\mathbf{r} \tag{40}$$

where $\eta_i^{(1,2)}(\mathbf{r})$ denotes the spatial profile of nonlinear polarization. In the time-domain Eq. (36) becomes

$$-i\left[1 - \frac{dk_{m,i}(K_i)}{dk}\right]\frac{d\mathrm{E}_{ip}}{dt} + \left[k_{m,i}(K_i) - K_i\right]\mathrm{E}_{ip} = \sum_{p_1}\left(V_{ip,ip_1}^{(1)} + V_{ip,ip_1}^{(2)}\right)\mathrm{E}_{ip_1} \tag{41}$$

$\eta_i^{(1,2)}(\mathbf{r})$ up to the 3${}^{\mathrm{rd}}$ order of nonlinearity is defined as follows [4]:

$$\eta_i^{(1,2)} = 2i\hbar\gamma_\parallel \Delta n_0^{(i)} D(K_i) A\left\{1 + 2A\sum_{i_1=1}\left|E_{i_1}^{(1,2)}\right|^2 \mathrm{Re}\left[D\left(K_{i_1}\right)\right]\right.$$
$$\left. + A\sum_{i_1\neq i}\left|E_{i_1}^{(1,2)}\right|^2 D_\parallel\left(K_i - K_{i_1}\right)\left[D(K_i) + D^*\left(K_{i_1}\right)\right]\right\} \tag{42}$$

where

$$A = -\frac{d^2}{2\hbar^2\gamma_\perp\gamma_\parallel}; \quad D(k) = \left(1 - i\frac{k-k_0}{\gamma_\perp}\right)^{-1}; \quad D_\parallel(k) = \left(1 - i\frac{k}{\gamma_\parallel}\right)^{-1} \tag{43}$$

$\Delta n_o^{(i)}$ is the population imbalance between the two levels responsible for the lasing in each disk, and k_0, $\gamma_\perp$, and $\gamma_\parallel$ represent frequency of the lasing transition, dephasing and population relaxation rates of the gain medium, respectively and d is the dipole matrix element of the transition. First we separate it into linear and nonlinear parts:

$$\eta_i^{(1,2)} = \eta_{i,1}^{(1,2)} + \eta_{i,3}^{(1,2)} \tag{44}$$

where

$$\eta_{i,1}^{(1,2)} = 2i\hbar\gamma_{\parallel}\Delta n_0^{(i)}D(K_i)A = -i\frac{d^2}{\hbar\gamma_{\perp}}\Delta n_0^{(i)}D(K_i)$$

$$\eta_{i,3}^{(1,2)} = i\Delta n_0^{(i)}D(K_i)\frac{1}{2\hbar\gamma_{\parallel}}\left(\frac{d^2}{\hbar\gamma_{\perp}}\right)^2\left\{2A\sum_{i_1=1}\left|E_{i_1}^{(1,2)}\right|^2\mathrm{Re}\left[D\left(K_{i_1}\right)\right]\right.$$

$$\left. +A\sum_{i_1\neq i}\left|E_{i_1}^{(1,2)}\right|^2 D_{\parallel}\left(K_i-K_{i_1}\right)\left[D(K_i)+D^*\left(K_{i_1}\right)\right]\right\}$$

(45)

Respectively, polarization matrix $V_{ip,ip_1}^{(1,2)}$ is also divided in two parts

$$V_{ip,ip_1}^{(1,2)} = -i\frac{2\pi k_0}{n_d^2}\frac{d^2}{\hbar\gamma_{\perp}}\Delta n_0^{(i)}D(K_i)\delta_{pp_1} + i\frac{\pi k_0\Delta n_0^{(i)}}{n_d^2}\frac{D(K_i)}{\hbar\gamma_{\parallel}}\left(\frac{d^2}{\hbar\gamma_{\perp}}\right)^2\iint_{D_1}{}^{\dagger}F_{i,p}^{(1,2)}(\mathbf{r})F_{i,p_1}^{(1,2)}(\mathbf{r})$$

$$\times\left\{2\sum_{i_1=1}\left|E_{i_1}^{(1,2)}\right|^2\mathrm{Re}\left[D\left(K_{i_1}\right)\right]+\sum_{i_1\neq i}\left|E_{i_1}^{(1,2)}\right|^2 D_{\parallel}\left(K_i-K_{i_1}\right)\left[D(K_i)+D^*\left(K_{i_1}\right)\right]\right\}d\mathbf{r}$$

(46)

so that Eq. (41) can be rewritten as

$$\left[1-\frac{dk_{m,i}(K_i)}{dk}\right]\frac{dE_{ip}}{dt}+i\left[k_{m,i}(K_i)-K_i+\frac{2\pi ik_0}{n_d^2}\frac{d^2}{\hbar\gamma_{\perp}}\Delta n_0 D(K_l)\right]E_{ip}$$

$$=\sum_{p_1}\left(W_{ip,ip_1}^{(1)}+W_{ip,ip_1}^{(2)}\right)E_{ip_1}$$

(47)

where $\Delta n_0 = \Delta n_0^{(1)}+\Delta n_0^{(2)}$ and we introduced

$$W_{ip,ip_1}^{(1,2)} = -\frac{\pi k_0\Delta n_0^{(i)}}{n_d^2}\frac{D(K_l)}{\hbar\gamma_{\parallel}}\left(\frac{d^2}{\hbar\gamma_{\perp}}\right)^2\iint_{D_1}{}^{\dagger}F_{i,p}^{(1,2)}(\mathbf{r})F_{i,p_1}^{(1,2)}(\mathbf{r})$$

$$\times\left\{2\sum_{i_1=1}\left|E_{i_1}^{(1,2)}\right|^2\mathrm{Re}\left[D\left(K_{i_1}\right)\right]+\sum_{i_1\neq i}\left|E_{i_1}^{(1,2)}\right|^2 D_{\parallel}\left(K_i-K_{i_1}\right)\left[D(K_i)+D^*\left(K_{i_1}\right)\right]\right\}d\mathbf{r}$$

(48)

Now we take into account (37) to get

$$W_{ip,ip_1}^{(1,2)} = -\frac{\pi k_0\Delta n_0^{(i)}}{n_d^2}\frac{D(K_i)}{\hbar\gamma_{\parallel}}\left(\frac{d^2}{\hbar\gamma_{\perp}}\right)^2$$

$$\times\sum_{i_1}\sum_{p_2 p_3}B_{i_1 p_2;i_1 p_3}^{(1,2)i,p;i,p_1}\left(2\mathrm{Re}\left[D\left(K_{i_1}\right)\right]+\left(1-\delta_{ii_1}\right)D_{\parallel}\left(K_i-K_{i_1}\right)\left[D(K_i)+D^*\left(K_{i_1}\right)\right]\right)E_{i_1 p_2}E_{i_1 p_3}^*$$

(49)

where we introduced integrals

$$B_{i_1 p_2;i_1 p_3}^{(1,2)i,p;i,p_1} = \int{}^{\dagger}F_{i,p}^{(1,2)}(\mathbf{r})F_{i,p_1}^{(1,2)}(\mathbf{r})F_{i_1 p_2}^{(1,2)}(\mathbf{r})\left[F_{i_1 p_3}^{(1,2)}(\mathbf{r})\right]^* d\mathbf{r}$$

(50)

It is convenient to present the modal functions in the following form:

$$
\begin{aligned}
F_{1,1}^{(1)} &= R^{-1}e^{im\varphi}Y_1^{(1)}(r); \quad F_{1,1}^{(2)} = R^{-1}e^{-im\varphi}Y_1^{(2)}(r); \\
F_{1,2}^{(1)} &= (-1)^m R^{-1}e^{-im\varphi}Y_1^{(1)}(r); \quad F_{1,2}^{(2)} = (-1)^m R^{-1}e^{im\varphi}Y_1^{(2)}(r) \\
F_{2,1}^{(1)} &= e^{im\varphi}R^{-1}Y_2^{(1)}(r); \quad F_{2,1}^{(2)} = R^{-1}e^{-im\varphi}Y_2^{(2)}(r); \\
F_{2,2}^{(1)} &= (-1)^m R^{-1}e^{-im\varphi}Y_2^{(1)}(r); \quad F_{2,2}^{(2)} = (-1)^m R^{-1}e^{im\varphi}Y_2^{(2)}(r)
\end{aligned}
\tag{51}
$$

where functions $Y_{1,2}^{(1,2)}$ are defined by comparing Eq. (51) to Eq. (20) - (23). Most of the coefficients $B_{i_1 p_2;i_1 p_3}^{(1,2)i,p;i,p_1}$ turn zero because of the integration over angle φ. The only non-zero coefficients are (Self-satuiration)

$$
B_{1,1;1,1}^{1,2;1,2} = B_{1,2;1,1}^{1,2;1,1} = B_{1,1;1,2}^{1,1;1,2} = B_{1,2;1,2}^{1,1;1,1} = B_{1,2;1,2}^{1,2;1,2} = B_{1,1;1,1}^{1,1;1,1} = \frac{1}{R^2}b_{11}^{(1,2)}
$$

$$
B_{2,1;2,1}^{2,2;2,2} = B_{2,2;2,1}^{2,2;2,1} = B_{2,1;2,2}^{2,1;2,2} = B_{2,2;2,2}^{2,1;2,1} = B_{2,2;2,2}^{2,2;2,2} = B_{2,1;2,1}^{2,1;2,1} = \frac{1}{R^2}b_{22}^{(1,2)}
\tag{52}
$$

where

$$
b_{11}^{(1,2)} = \frac{2\pi}{R^2}\int_0^{R_{1,2}} drr\left[Y_1^{(1,2)}\right]^2\left|Y_1^{(1,2)}\right|^2; \quad b_{22}^{(1,2)} = \frac{2\pi}{R^2}\int_0^{R_{1,2}} drr\left[Y_2^{(1,2)}\right]^2\left|Y_2^{(1,2)}\right|^2
\tag{53}
$$

For cross-saturation terms we have similalry

$$
B_{2,1;2,1}^{1,2;1,2} = B_{2,2;2,1}^{1,2;1,1} = B_{2,1;2,2}^{1,1;1,2} = B_{2,2;2,2}^{1,1;1,1} = B_{2,2;2,2}^{1,2;1,2} = B_{2,1;2,1}^{1,1;1,1} = \frac{1}{R^2}b_{12}^{(1,2)}
$$

$$
B_{1,1;1,1}^{2,2;2,2} = B_{1,2;1,1}^{2,2;2,1} = B_{1,1;1,2}^{2,1;2,2} = B_{1,2;1,2}^{2,1;2,1} = B_{1,2;1,2}^{2,2;2,2} = B_{1,1;1,1}^{2,1;2,1} = \frac{1}{R^2}b_{21}^{(1,2)}
\tag{54}
$$

where

$$
b_{12}^{(1,2)} = \frac{2\pi}{R^2}\int_0^{R_{1,2}} drr\left[Y_1^{(1,2)}\right]^2\left|Y_2^{(1,2)}\right|^2; \quad b_{21}^{(1,2)} = \frac{2\pi}{R^2}\int_0^{R_{1,2}} drr\left[Y_2^{(1,2)}\right]^2\left|Y_1^{(1,2)}\right|^2
\tag{55}
$$

The system of lasing equations for modal amplitudes can now be presented in the following form

$$
\frac{d\mathrm{E}_{1,1}}{dt} + i\left[k_1(K_1) - K_1 + \frac{2\pi i k_0}{n_d^2}\frac{d^2}{\hbar\gamma_\perp}\Delta n_0 D(K_1)\right]\mathrm{E}_{1,1} =
$$

$$
b_{11}h_{11}\mathrm{E}_{1,1}\left(\left|\mathrm{E}_{1,1}\right|^2 + 2\left|\mathrm{E}_{1,2}\right|^2\right) + b_{12}h_{12}\left(\mathrm{E}_{1,1}\left|\mathrm{E}_{2,1}\right|^2 + \mathrm{E}_{1,1}\left|\mathrm{E}_{2,2}\right|^2 + \mathrm{E}_{1,2}\mathrm{E}_{2,2}^*\mathrm{E}_{2,1}\right)
\tag{56}
$$

$$\frac{d\mathrm{E}_{1,2}}{dt} + i\left[k_1(K_1) - K_1 + \frac{2\pi i k_0}{n_d^2}\frac{d^2}{\hbar\gamma_\perp}\Delta n_0 D(K_1)\right]\mathrm{E}_{1,2} =$$

$$h_{11}b_{11}\mathrm{E}_{1,2}\left(2|\mathrm{E}_{1,1}|^2 + |\mathrm{E}_{1,2}|^2\right) + h_{12}b_{12}\mathrm{E}_{1,2}\left(\mathrm{E}_{1,2}|\mathrm{E}_{2,1}|^2 + \mathrm{E}_{1,2}|\mathrm{E}_{2,2}|^2 + \mathrm{E}_{1,1}\mathrm{E}_{2,2}\mathrm{E}_{2,1}^*\right)$$

(57)

$$\frac{d\mathrm{E}_{2,1}}{dt} + i\left[k_2(K_2) - K_2 + \frac{2\pi i k_0}{n_d^2}\frac{d^2}{\hbar\gamma_\perp}\Delta n_0 D(K_2)\right]\mathrm{E}_{2,1} =$$

$$h_{22}b_{22}\mathrm{E}_{2,1}\left(|\mathrm{E}_{2,1}|^2 + 2|\mathrm{E}_{2,2}|^2\right) + h_{21}b_{21}\left(\mathrm{E}_{2,1}|\mathrm{E}_{1,1}|^2 + \mathrm{E}_{2,1}|\mathrm{E}_{1,2}|^2 + \mathrm{E}_{2,2}\mathrm{E}_{1,1}\mathrm{E}_{1,2}^*\right)$$

(58)

$$\frac{d\mathrm{E}_{2,2}}{dt} + i\left[k_2(K_2) - K_2 + \frac{2\pi i k_0}{n_d^2}\frac{d^2}{\hbar\gamma_\perp}\Delta n_0 D(K_2)\right]\mathrm{E}_{2,2} =$$

$$b_{22}h_{22}\mathrm{E}_{2,2}\left(2|\mathrm{E}_{21}|^2 + |\mathrm{E}_{22}|^2\right) + b_{21}h_{21}\left(\mathrm{E}_{2,2}|\mathrm{E}_{11}|^2 + \mathrm{E}_{2,2}|\mathrm{E}_{12}|^2 + \mathrm{E}_{2,1}\mathrm{E}_{1,2}\mathrm{E}_{1,1}^*\right)$$

(59)

where we introduced notations

$$h_{11} = -\frac{2\pi k_0}{n_d^2}\frac{D(K_1)}{\hbar\gamma_\parallel}\left(\frac{d^2}{\hbar\gamma_\perp R}\right)^2\mathrm{Re}\left[D(K_1)\right]$$

$$h_{22} = -\frac{2\pi k_0}{n_d^2}\frac{D(K_2)}{\hbar\gamma_\parallel}\left(\frac{d^2}{\hbar\gamma_\perp R}\right)^2\mathrm{Re}\left[D(K_2)\right]$$

$$h_{12} = -\frac{\pi k_0}{n_d^2}\frac{D(K_1)}{\hbar\gamma_\parallel}\left(\frac{d^2}{\hbar\gamma_\perp R}\right)^2\left(2\mathrm{Re}\left[D(K_2)\right] + D_\parallel(K_1 - K_2)\left[D(K_1) + D^*(K_2)\right]\right)$$

$$h_{21} = -\frac{\pi k_0}{n_d^2}\frac{D(K_2)}{\hbar\gamma_\parallel}\left(\frac{d^2}{\hbar\gamma_\perp R}\right)^2\left(2\mathrm{Re}\left[D(K_1)\right] + D_\parallel(K_2 - K_1)\left[D(K_2) + D^*(K_1)\right]\right)$$

(60)

and

$$b_{ij} = \Delta n_0^{(1)}b_{ij}^{(1)} + \Delta n_0^{(2)}b_{ij}^{(2)}$$

(61)

We also neglected the derivative of the eigenfrequency with respect to the spectral parameters, which is allowed for high-Q resonators. Eq.(56) and Eq. (57) describe dynamics of the field in the first pair of degenerate modes, while Eq. (58) and (59) deal with the second pair.   In the case of the single mode lasing, only one of these pairs have non-zero field. For instance, we can choose $\mathrm{E}_{2,1} = \mathrm{E}_{2,2} = 0$, in which case Eq. (56) and (57) reduce to

$$\frac{d\mathrm{E}_{1,1}}{dt} + i\left[k_1(K_1) - K_1 + \frac{2\pi i k_0}{n_d^2}\frac{d^2}{\hbar\gamma_\perp}\Delta n_0 D(K_1)\right]\mathrm{E}_{1,1} = b_{11}h_{11}\mathrm{E}_{1,1}\left(|\mathrm{E}_{1,1}|^2 + 2|\mathrm{E}_{1,2}|^2\right)$$

$$\frac{d\mathrm{E}_{1,2}}{dt} + i\left[k_1(K_1) - K_1 + \frac{2\pi i k_0}{n_d^2}\frac{d^2}{\hbar\gamma_\perp}\Delta n_0 D(K_1)\right]\mathrm{E}_{1,2} = h_{11}b_{11}\mathrm{E}_{1,2}\left(2|\mathrm{E}_{1,1}|^2 + |\mathrm{E}_{1,2}|^2\right)$$

(62)

Eq. (62) shows that the degenerate modes cross-saturate each other with the coefficient of cross saturation two times larger than that of self-saturation. Therefore, assuming that one of the modes starts lasing first it will saturate population inversion for the second mode suppressing its lasing. Since both degenerate modes have the same threshold, one can assume that only one of those modes will play a role in the devices under construction.

Therefore, we can assume that the two-mode lasing is only possible with non-degenerate modes, i.e. $E_{1,1}$ and $E_{2,1}$, we can study the mode dynamics with reduced equations

$$\frac{dE_{1,1}}{dt} + i\left[k_1(K_1) - K_1 + \frac{2\pi i k_0}{n_d^2} \frac{d^2}{\hbar\gamma_\perp} \Delta n_0 D(K_1) \right] E_{1,1} = b_{11}h_{11}E_{1,1}\left|E_{1,1}\right|^2 + b_{12}h_{12}E_{1,1}\left|E_{2,1}\right|^2$$

$$\frac{dE_{2,1}}{dt} + i\left[k_2(K_2) - K_2 + \frac{2\pi i k_0}{n_d^2} \frac{d^2}{\hbar\gamma_\perp} \Delta n_0 D(K_2) \right] E_{2,1} = h_{22}b_{22}E_{2,1}\left|E_{2,1}\right|^2 + h_{21}b_{21}E_{2,1}\left|E_{1,1}\right|^2$$

(63)

Presenting field in the form $E_{i,1} = \left|E_i\right|\exp(-i\psi_i)$ and separating real and imaginary parts of (63) we have equations for intensity

$$\dot{I}_1 = 2I_1\left(\xi_1(K_1) + \mathrm{Re}[b_{11}h_{11}]I_1 + \mathrm{Re}[b_{12}h_{12}]I_2\right)$$

$$\dot{I}_2 = 2I_2\left(\xi_2(K_2) + \mathrm{Re}[b_{22}h_{22}]I_2 + \mathrm{Re}[b_{21}h_{21}]I_2\right)$$

(64)

and phase

$$\dot{\psi}_1 - \sigma_1 + K_1 = -\mathrm{Im}[b_{11}h_{11}]I_1 - \mathrm{Im}[b_{12}h_{12}]I_2$$

$$\dot{\psi}_2 - \sigma_2 + K_2 = -\mathrm{Im}[b_{11}h_{11}]I_1 - \mathrm{Im}[b_{12}h_{12}]I_2$$

(65)

where

$$k_{1,2}(K_{1,2}) + \frac{2\pi i k_0}{n_d^2} \frac{d^2}{\hbar\gamma_\perp} \Delta n_0 D(K_{1,2}) = \sigma_{1,2}(K_{1,2}) + i\xi_{1,2}(K_{1,2})$$

(66)

$$I_{1,2} = \left|E_{1,2}\right|^2$$

$$\sigma_i = k_i' - \frac{2\pi k_0 d^2 \Delta n_0}{\hbar n_d^2} \frac{K_i - k_0}{(K_i - k_0)^2 + \gamma_\perp^2}$$

$$\xi_i = -k_i'' + \frac{2\pi k_0 d^2 \Delta n_0}{\hbar n_d^2} \frac{\gamma_\perp}{(K_i - k_0)^2 + \gamma_\perp^2}$$

(67)

The effective coupling coefficient determining stability of various lasing regimes in this case is given by

$$C = \frac{\mathrm{Re}[h_{12}b_{12}]\mathrm{Re}[h_{21}b_{21}]}{\mathrm{Re}[h_{11}b_{11}]\mathrm{Re}[h_{22}b_{22}]}$$

(68)

Neglecting population pulsation terms in (60) we have

$$h_{11} = -\frac{2\pi k_0}{n_d^2} \frac{1}{\hbar\gamma_\parallel} \left(\frac{d^2}{\hbar\gamma_\perp R}\right)^2 D(K_1)\text{Re}\left[D(K_1)\right]$$

$$h_{22} = -\frac{2\pi k_0}{n_d^2} \frac{1}{\hbar\gamma_\parallel} \left(\frac{d^2}{\hbar\gamma_\perp R}\right)^2 D(K_2)\text{Re}\left[D(K_2)\right]$$

$$h_{12} = -\frac{2\pi k_0}{n_d^2} \frac{1}{\hbar\gamma_\parallel} \left(\frac{d^2}{\hbar\gamma_\perp R}\right)^2 D(K_1)\text{Re}\left[D(K_2)\right]$$

(69)

$$h_{21} = -\frac{\pi k_0}{n_d^2} \frac{1}{\hbar\gamma_\parallel} \left(\frac{d^2}{\hbar\gamma_\perp R}\right)^2 D(K_2)\text{Re}\left[D(K_1)\right]$$

and

$$C = \frac{\text{Re}\left[D(K_1)b_{12}\right]\text{Re}[D(K_2)b_{21}]}{\text{Re}[D(K_1)b_{11}]\text{Re}[D(K_2)b_{22}]}$$

(70)

Behavior of the laser depends on the parameters $\xi_1(K_1)$, $\xi_2(K_2)$: the lasing begins, when one of these parameters becomes greater than zero. In the single mode regime, when only one mode lazes, we have

$$\dot{I}_i = 2I_i\left(\xi_i(K_i) + \text{Re}\left[b_{ii}h_{ii}\right]I_i\right)$$

$$K_i = \sigma_i - \text{Im}\left[b_{ii}h_{ii}\right]I_i$$

(71)

Consider

$$h_{ii} = -\frac{2\pi k_0}{n_d^2} \frac{1}{\hbar\gamma_\parallel} \left(\frac{d^2}{\hbar\gamma_\perp R}\right)^2 D(K_i)\text{Re}\left[D(K_i)\right];$$

$$\text{Re}\left[D(K_i)\right] = \left(1 - i\frac{k-k_0}{\gamma_\perp}\right)^{-1} = \frac{(\gamma_\perp)^2}{(\gamma_\perp)^2 + (K_i - k_0)^2} = g(K_i)$$

(72)

$$\text{Im}\left[D(K_i)\right] = \frac{\gamma_\perp(K_i - k_0)}{(\gamma_\perp)^2 + (K_i - k_0)^2} = f(K_i)$$

Lasing threshold is defined as

$$\Delta n_0^{(i)} = \frac{(K_i - k_0)^2 + \gamma_\perp^2}{\gamma_\perp} \frac{\hbar n_d^2 k_i''}{2\pi k_0 d^2} = \frac{\hbar n_d^2 \gamma_\perp}{2\pi k_0 d^2} k_i'' \left[1 + \frac{\left(k_i'(K_i) - k_0\right)^2}{\left(\gamma_\perp + k_i''(K_i)\right)^2}\right]$$

(73)

where we used equation for the lasing frequency at the threshold

$$K_i = \frac{\gamma_\perp k_i'(K_i) + k_0 k_i''(K_i)}{\gamma_\perp + k_i''(K_i)}$$

$$K_i - k_0 = \frac{\gamma_\perp k_i'(K_i) + k_0 k_i''(K_i)}{\gamma_\perp + k_i''(K_i)} - k_0 = \gamma_\perp \frac{k_i'(K_i) - k_0}{\gamma_\perp + k_i''(K_i)}$$

(74)

It is important to determine, which mode has a lower threshold, while the absolute threshold value is not important. Thus we can define the "threshold coefficient"

$$\psi_{th} = \frac{\hbar n_d^2 \gamma_\perp}{2\pi k_0 d^2 R}$$

(75)

Defining thresholds normalized by ψ_{th} we have

$$\Delta \tilde{n}_0^{(i)} = \gamma_i \left[1 + \frac{(x_i - x_0)^2}{(\gamma_\perp + \gamma_i)^2} \right]$$

(76)

Where all x_i and γ_i are dimensionless real and imaginary parts of the eigenfrequency of the respective mode, calculated at the lasing frequency, x_0 and $\gamma_\perp$ are dimensionless atomic frequency and gain width respectively. Dimensionless equation for the threshold lasing frequency is

$$X_i = \frac{\gamma_\perp x_i(X_i) + x_0 \gamma_i(X_i)}{\gamma_\perp + \gamma_i(X_i)}$$

(77)

In the stationary single mode state:

$$I_i = -\frac{\xi_i(K_i)}{\mathrm{Re}[b_{ii} h_{ii}]} = \frac{R^2 \hbar^2 \gamma_\perp \gamma_\parallel}{d^2} \frac{\Delta n_0 - \Delta n_0^{(th)}}{\mathrm{Re}[b_{ii} D(K_i)]}$$

$$\tilde{I}_i = \frac{\Delta n_0 - \Delta n_0^{(th)}}{\mathrm{Re}[b_{ii} D(K_i)]}; \tilde{I}_i = I_i \frac{d^2}{R^2 \hbar^2 \gamma_\perp \gamma_\parallel}$$

(78)

where we introduced dimensionless intensity. For the stationary single mode frequency we have equation:

$$X_i = \sigma_i + \xi_i \frac{\mathrm{Im}[b_{ii} h_{ii}]}{\mathrm{Re}[b_{ii} h_{ii}]} = \sigma_i + \xi_i \frac{\mathrm{Im}[b_{ii} D(X_i)]}{\mathrm{Re}[b_{ii} D(X_i)]}$$

(79)

where σ_i and ξ_i can be rewritten as

$$\sigma_i = k_i' - \Delta \tilde{n}_0 f(X_i)$$

$$\xi_i = \left(\Delta \tilde{n}_0 - \Delta \tilde{n}_0^{th} \right) g(X_i)$$

(80)

and

$$D(k) = g(X_i) + if(X_i)$$

$$g(X_i) = \frac{(\gamma_\perp)^2}{(\gamma_\perp)^2 + (X_i - x_0)^2}; f(X_i) = \frac{\gamma_\perp (X_i - x_0)}{(\gamma_\perp)^2 + (X_i - x_0)^2} \tag{81}$$

The derived formulas lay foundation for the analysis of laser's behavior for various parameters of the system and for design of the desirable bistable behavior.

References

[1]   H. E. Türeci, a D. Stone, L. Ge, S. Rotter, and R. J. Tandy, Nonlinearity **22**, C1-C18 (2009).
[2]   H. Türeci, a. Stone, and L. Ge, Physical Review A **76**, 1-4 (2007).
[3]   M. Abramowitz and I. A. Stegun, *Handbook of Mathematical Functions with Formulas, Graphs, and Mathematical Tables* (U.S. Govt. Print. Off., Washington,, 1964), p. xiv, 1046 p.
[4]   O. Zaitsev and L. Deych, Physical Revew A **81**, 23822 (2010).